applied sciences

MDPI

Article

Cyclic Shear Behavior of Co-Extruded Geomembrane–Geotextile Interfaces Under Horizontal Cyclic Loading

Juan Hou [1,2,*], Hanru Feng [1] and Yanxia Ma [2]

[1] School of Mechanics and Engineering Science, Shanghai University, Shanghai 200444, China; 22723966@shu.edu.cn
[2] School of Civil Engineering and Water Resources, Qinghai University, Xining 810016, China; 2001990020@qhu.edu.cn
* Correspondence: juanhou@staff.shu.edu.cn

Abstract

The cyclic shear behavior of geomembrane (GM)–geotextile (GT) interfaces is critical to the seismic stability and containment performance of composite bottom liners. This study quantified the cyclic shear behavior of co-extruded textured geomembrane (GMTC)–nonwoven geotextile (NWGT) interfaces through 27 large-scale horizontal cyclic shear tests conducted under normal stresses (σ_n) of 100, 200, and 400 kPa, displacement amplitudes (A) of 5, 10, and 20 mm, and shear frequencies (f) of 0.5, 1.0, and 2.0 Hz, with 60 loading cycles applied to each test. The results show that the cyclic shear response varied substantially with normal stress. At f = 0.5 Hz, peak cyclic shear resistance increased with normal stress, whereas the 60th-cycle strength-retention ratio generally decreased, indicating a larger relative difference between the maximum measured cyclic shear resistance and the 60th-cycle resistance under higher confinement conditions. The measured peak cyclic shear resistance varied with displacement amplitude in a normal-stress-dependent manner. At 100 kPa, the measured peak resistances at 5 and 10 mm were similar, with a higher value at 20 mm, whereas at 200 and 400 kPa, the values at 5 and 10 mm were similar and were lower at 20 mm. The fitted peak friction angles at 5 and 10 mm were similar and lower at 20 mm. The calculated cyclic secant stiffness decreased by approximately 30–35% after 60 cycles at f = 0.5 Hz. Under a normal stress of 400 kPa and a displacement amplitude of 5 mm, the measured peak cyclic shear resistance differed among the tested coupled frequency–velocity conditions. At σ_n = 400 kPa and A = 20 mm, post-test photographs showed different surface conditions among the tested coupled frequency–velocity conditions, including surface scratching, detached particles, and more pronounced fiber attachment at 2.0 Hz. The findings suggest that dynamic interface performance should be evaluated using not only peak cyclic shear resistance but also cyclic resistance degradation, stiffness reduction, damping evolution, and surface characteristics.

Keywords: geomembrane; geotextile; horizontal cyclic shear test; cyclic interfacial shear performance; stiffness degradation; damping ratio

Check for updates

Academic Editor: Marco Zucca

Received: 15 September 2026
Revised: 1 October 2026
Accepted: 2 October 2026
Published: 7 October 2026

Copyright: © 2026 by the authors. Licensee MDPI, Basel, Switzerland. This article is an open access article distributed under the terms and conditions of the Creative Commons Attribution (CC BY) license.

1. Introduction

Geosynthetic composite liners are widely used in waste containment facilities, and interface stability is essential for maintaining liner integrity under seismic loading [1–6]. Geomembranes (GMs) serve as a hydraulic barrier, whereas geotextiles (GTs) are commonly installed above GMs to protect them from puncture and local damage caused by overlaid

aggregate drainage layers and operational loading [7,8]. However, the contact between GMs and GTs often exhibits lower shear resistance than adjacent liner components, making the GM–GT interface a potential preferential sliding plane within composite liners [2–4,9,10]. Under waste placement, long-term settlement, leachate exposure, and earthquake-induced cyclic loading, progressive interface slip or strength degradation may compromise liner integrity and serviceability. Therefore, characterizing the cyclic shear behavior and post-test surface evolution of GM–GT interfaces is essential for performance-based design and seismic stability assessment of landfill barrier systems [1–3,11].

Previous studies have established that the monotonic shear behavior of GM–GT interfaces is strongly affected by geomembrane surface texture, asperity density, geotextile properties, and temperature. Jones and Dixon [10] reported that GM roughness affects the shear displacement required to reach peak strength, with smooth interfaces reaching peak strength within approximately 2 mm and textured interfaces requiring 5–10 mm displacements. Fowmes et al. [12] confirmed that interface shear strength increases with the density of geomembrane asperities. Karademir and Frost [13] found that temperature can affect the shear response of GM–GT interfaces, while Adeleke et al. [14] reported that greater geomembrane asperity height increased the peak interface friction angle, and Abdelaal and Solanki [15] found that the interface friction angle decreased with increasing geotextile mass per unit area. Recent studies have further quantified the asperity geometry of textured geomembranes and its evolution during interface shearing through pre- and post-shear surface characterization, covering impinged (GMTI), co-extruded (GMTC), and low- and high-asperity embossed ($GMTE_L$ and $GMTE_H$) geomembranes [16–18].

Although these studies provide important insights into monotonic interface resistance, monotonic shear tests cannot capture load reversal, cyclic degradation, and energy dissipation under earthquake-induced cyclic loading [3,11,19,20]. For dynamic interface assessment, hysteresis loops, backbone curves, shear stiffness, and equivalent viscous damping ratio have been widely used to describe cyclic shear response [3,11,19–21]. Cyclic shear studies have shown that normal stress, cycle number, displacement amplitude, and loading frequency significantly influence the dynamic behavior of geosynthetic interfaces [3,11,19–24]. For GM–GT interfaces, Chang and Feng [3] investigated the cyclic shear behavior of a GMTI–nonwoven geotextile (NWGT) interface under normal stresses of 100–1000 kPa, displacement amplitudes of 5–25 mm, and loading frequencies of 0.2–2.0 Hz over 60 loading cycles. Hou et al. [11] examined a GMTI–NWGT interface with a reported asperity height of 0.25 mm under normal stresses of 100–400 kPa and displacement amplitudes of 1–10 mm at a sliding rate of 2 mm/min for 10 cycles. Both studies evaluated cyclic shear resistance, stiffness, damping behavior, vertical deformation, and post-shear surface changes. More recently, Wu et al. [25] investigated the microscale cyclic shear behavior of a GMTE–NWGT interface using the discrete element method (DEM). Lin et al. [4] extended the scope of investigation from single interfaces to multilayer composite liners and showed that failure was concentrated along the GMTE–NWGT interface, indicating that single-interface tests may overestimate the shear capacity of composite liner systems. However, experimental cyclic characterization of GMTC–NWGT interfaces with integrally formed asperities under combined normal-stress, displacement-amplitude, and coupled frequency–velocity conditions remains limited, particularly with respect to cyclic shear resistance, stiffness, damping behavior, vertical response, and post-test surface characteristics. Without the data regarding such coupled cyclic responses, it is challenging to comprehensively characterize the horizontal dynamic shear behavior of GMTC–NWGT interfaces.

To address the research gap, 27 large-scale horizontal cyclic shear tests were conducted on GMTC–NWGT interfaces. The effects of normal stress (100, 200, and 400 kPa), displacement amplitude (5, 10, and 20 mm), and shear frequency (0.5, 1.0, and 2.0 Hz) were

evaluated over 60 cycles based on shear stress–displacement response, peak and 60th-cycle cyclic shear resistance, the 60th-cycle strength-retention ratio, shear stiffness, equivalent damping ratio, vertical displacement, and post-test surface observations. The mechanical response and post-test surface evolution under high-frequency and large-displacement loading were also examined. Accordingly, this study characterizes the cyclic response of the tested GMTC–NWGT interface across 27 combinations of normal stress, displacement amplitude, and coupled frequency–velocity conditions.

2. Materials and Methods

2.1. Materials and Apparatus

The NWGT used in the horizontal cyclic shear tests was composed of 100% virgin polypropylene fibers bonded by needle punching (Figure 1a), consistent with the standard material used in landfill liner systems. The basic properties of the NWGT, including thickness, mass per unit area, and tensile strength, are summarized in Table 1.

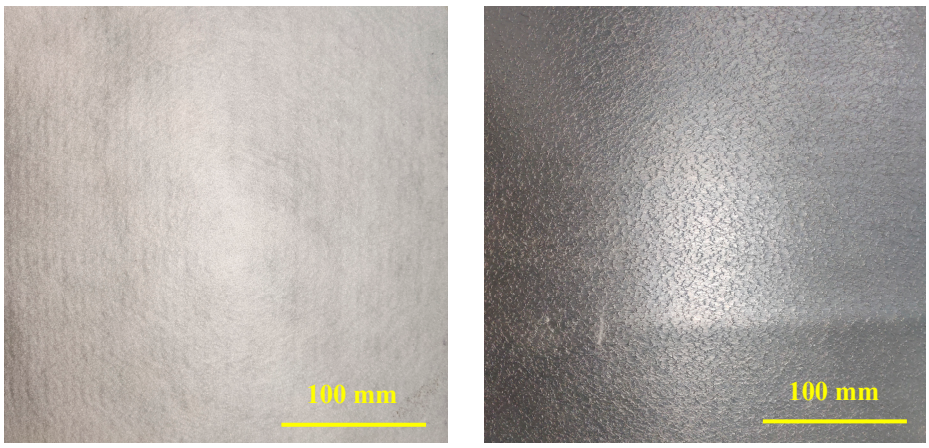

(**a**) (**b**)

Figure 1. Photographs of materials used in large-scale dynamic shear tests: (**a**) nonwoven geotextile (NWGT); (**b**) co-extruded textured geomembrane (GMTC).

Table 1. Physical and mechanical properties of NWGTs used in large-scale dynamic shear tests.

Thickness (mm)	Mass Per Unit Area (g/m^2)	Tensile Strength (kN/m)	CBR Puncture Resistance (kN)	Pyramid Puncture (kN)	Elongation at Break (%)
2	400	31	5.1	0.425	75

The geomembrane was made of HDPE and featured a co-extruded textured surface (GMTC; Figure 1b), which was used as the paired material in the interface tests. The GMTC had an asperity height of 0.4 mm. This asperity height falls within the common range of asperity heights for GMTC used in practice. The GMTC had a nominal thickness of 2.0 mm, which is the standard thickness for geomembranes used in landfill liners. The basic properties of the GMTC are summarized in Table 2.

Table 2. Physical and mechanical properties of GMTCs used in large-scale dynamic shear tests.

Thickness (mm)	Asperity Height (mm)	Density (kg/m^3)	Tensile Strength at Yield (N/mm)	Tensile Elongation at Yield or Break (%)	Puncture Strength (N)
2	0.4	940	30	12	600

A large-scale dynamic shear apparatus (Popwil ECE. Co., Hangzhou, China) was used for testing, as shown in Figure 2a. The upper shear box measured 305 mm × 305 mm, and the lower shear box measured 505 mm × 305 mm. Special gripping plates with diamond-shaped protrusions were mounted on the upper and lower shear boxes, while the NWGT and GMTC specimens were fixed to the upper and lower gripping plates, respectively (see Figure 2b). The horizontal servo actuator connected to the lower shear box provided a horizontal push or pull force of 0–35 kN, while the normal servo actuator connected to the upper shear box provided a normal loading range of 0–60 kN. The apparatus had a maximum shear displacement of 100 mm and a maximum displacement amplitude of ±25 mm. The cyclic loading frequency range was 0–5 Hz. The test-force accuracy was within 0.5%, the displacement measurement resolution was 0.01 mm, and the data were recorded at a sampling interval of 10 ms.

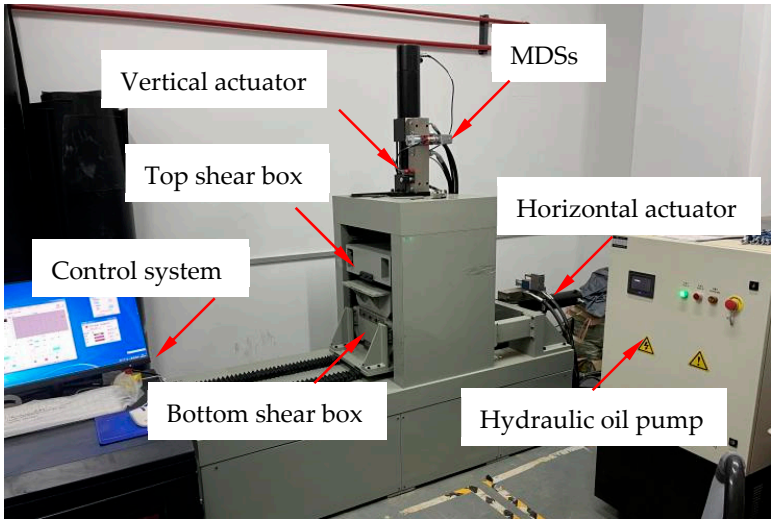

(**a**)

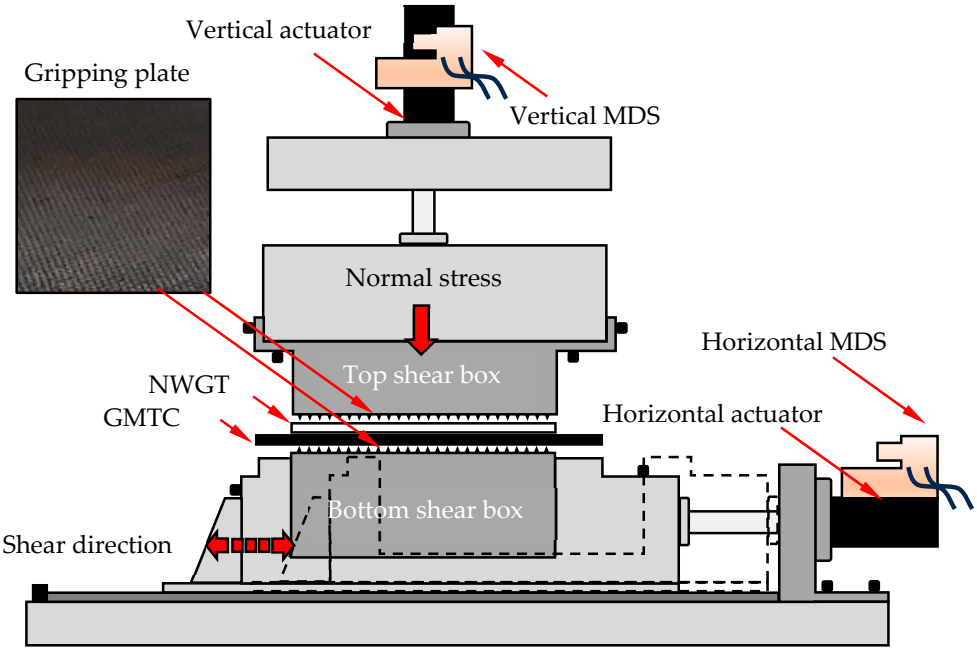

(**b**)

Figure 2. Large-scale dynamic shear apparatus used in a testing program: (**a**) photograph; (**b**) schematic diagram.

2.2. Methods

The test apparatus, specimen installation, and load application were carried out in accordance with ASTM D5321(2014) [26]. GMTC and NWGT specimens were cut to dimensions of 505 mm × 305 mm and 305 mm × 305 mm, respectively, to maintain a constant shear contact area during cyclic shear testing. After the GMTC and NWGT specimens were fixed to the gripping plates, the normal load was applied at a constant rate of 50 kN/min. The steel gripping plate is a laboratory boundary condition that may restrain NWGT deformation differently from field conditions. The NWGT was in contact with the textured surface of the GMTC, representing the orientation commonly used in practice for landfill liner systems [3,9,10,15,27,28]. After the preset normal stress was reached, it was maintained for 10 min to allow specimen seating and stabilization of the normal load. The normal load was controlled in a closed-loop manner based on feedback from the load cell so that the normal stress was continuously maintained at the preset value. The initial horizontal and vertical displacements were then set to zero. The lower shear box was controlled by a horizontal actuator under closed-loop displacement control to apply cyclic loading in the horizontal direction.

To investigate the dynamic shear behavior of the GMTC–NWGT interface, a total of 27 displacement-controlled cyclic shear tests were conducted. The tests included three normal stresses (σ_n = 100, 200, and 400 kPa), three displacement amplitudes (A = 5, 10, and 20 mm), and three loading frequencies (f = 0.5, 1.0, and 2.0 Hz). The selected normal stresses, displacement amplitudes, and loading frequencies were based on previous cyclic shear and shaking-table studies to cover different confinement levels and a range of cyclic interface responses from limited interface slip to severe repeated sliding [3,11,19,29,30]. Each parameter combination was tested once, and independent repeat tests were not performed. Therefore, specimen-to-specimen and installation variability, as well as the repeatability of small differences between neighboring test conditions, could not be quantified.

Cyclic loading was applied for 60 cycles using the following sinusoidal waveform:

$$u(t) = A\sin(2\pi ft) \quad (1)$$

where A is the prescribed displacement amplitude, f is the frequency, and t is time. The nominal maximum sliding velocity corresponding to the prescribed sinusoidal input is calculated as:

$$v_{max} = 2\pi fA \quad (2)$$

Under the prescribed test conditions, the nominal maximum sliding velocity ranged from 15.7 to 251.3 mm/s. The three loading frequencies therefore correspond to different nominal maximum sliding velocities and are treated as coupled frequency–velocity conditions. Measured amplitudes, cyclic periods and errors for the 27 conditions are presented in Supplementary Table S1. Displacement–time and shear force–time histories for the representative conditions (400 kPa, 20 mm) are presented in Supplementary Figures S1 and S2.

All tests were conducted at room temperature (20 °C). Localized interfacial heating was not measured.

3. Results

3.1. Shear Stress–Displacement Relationships

Figure 3a shows that, at 100 kPa, the measured peak shear stresses at 5 and 10 mm were similar, at 61.5 and 63.2 kPa, respectively, while a higher value of 68.7 kPa was measured at 20 mm. At 200 kPa, similar peak shear stresses were measured at 5 and 10 mm (107.2 and 109.9 kPa), whereas a lower value of 88.9 kPa was measured at 20 mm. Similarly, at 400 kPa, the measured values at 5 and 10 mm were 198.5 and 203.6 kPa, and were considered similar,

while a lower value of 181.6 kPa was measured at 20 mm. The 60th-cycle cyclic shear resistance increased monotonically with increasing normal stress, ranging from 48.4 to 51.0 kPa at 100 kPa, 67.4 to 83.8 kPa at 200 kPa, and 128.3 to 130.7 kPa at 400 kPa. The hysteresis loop area increased with displacement amplitude.

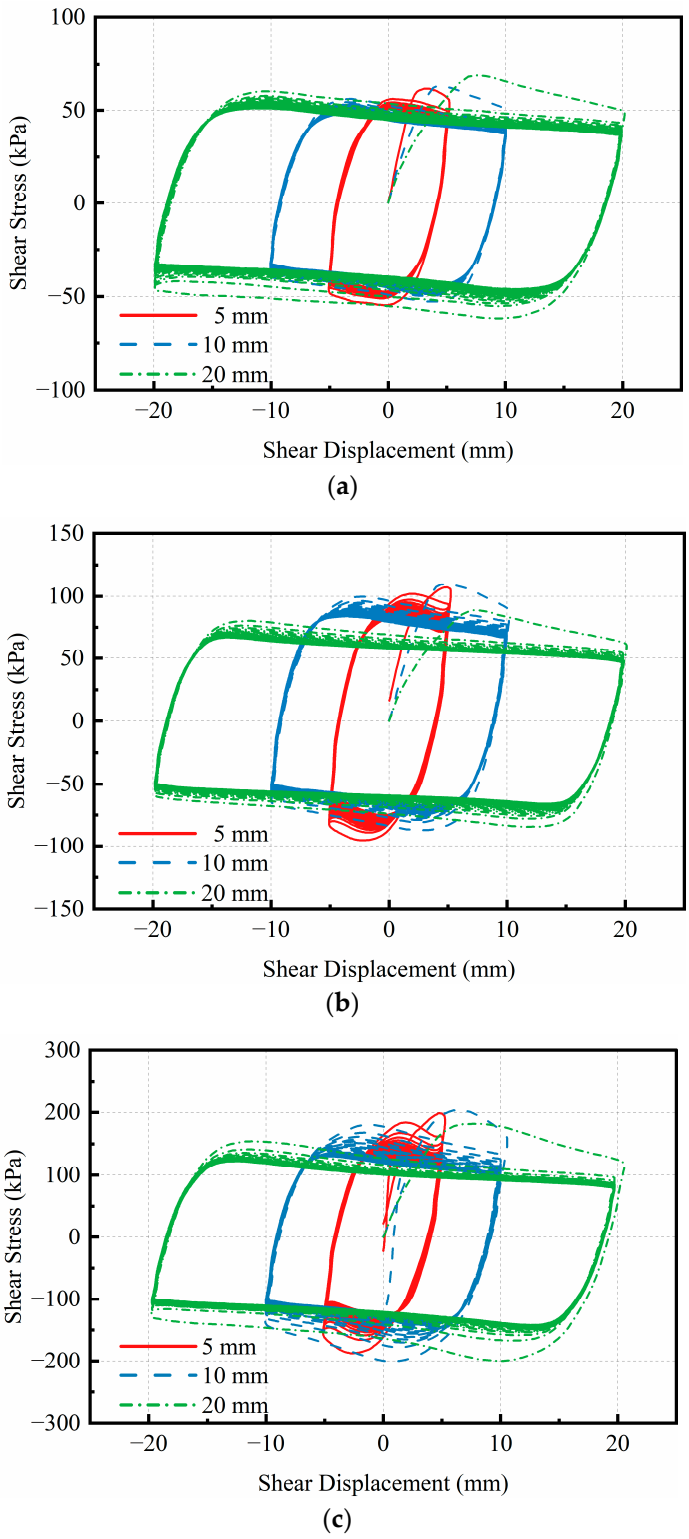

Figure 3. Shear stress vs. displacement of all 60 cycles under different displacement amplitudes at f = 0.5 Hz: (**a**) σ_n = 100 kPa; (**b**) σ_n = 200 kPa; (**c**) σ_n = 400 kPa.

Figure 4 presents a representative condition at σ_n = 400 kPa and A = 5 mm to compare the shear stress–displacement responses under the three loading frequencies. This condition was selected to illustrate the coupled frequency–velocity response under a fixed normal stress and displacement amplitude. Across the tested coupled frequency–velocity conditions, the positive-direction maximum shear stress in the first complete cycle after the displacement amplitude stabilized decreased from 198.5 kPa at 0.5 Hz (green dash-dotted curve, N = 1) to 178.2 kPa at 1.0 Hz (blue dashed curve, N = 3) and 161.3 kPa at 2.0 Hz (red solid curve, N = 5). The enclosed hysteresis loop area also decreased from 2274 kPa·mm (green dash-dotted curve) to 1910 kPa·mm (blue dashed curve) and 685 kPa·mm (red solid curve). At the beginning of the tests, particularly at the higher loading frequency (the red solid curve), the actuator response exhibited an initial stage in which the achieved displacement amplitude progressively increased, which may be associated with the inertial response of the loading system. During this stage, both the displacement amplitude and peak shear stress increased with cycle number, accompanied by an increase in the enclosed hysteresis-loop area. Once the achieved displacement amplitude reached a relatively stable level, the hysteresis-loop area also became comparatively stable.

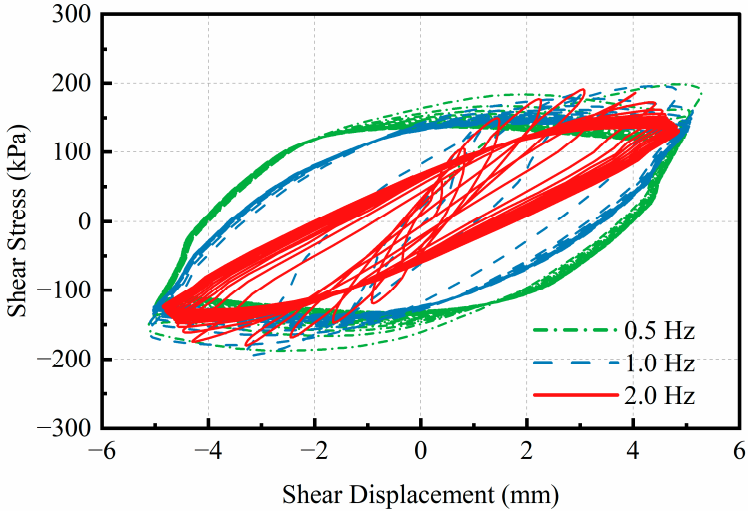

Figure 4. Representative shear stress–displacement curves of the GMTC–NWGT interface under different loading frequencies at σ_n = 400 kPa and A = 5 mm.

Figure 5 shows the backbone curves at N = 1, 2, 3, 5, 10, 30 and 60 cycles at σ_n = 400 kPa. The red arrows denote shear hardening, while the blue arrows indicate shear softening. Their positions and lengths represent the occurrence and duration of these behaviors during cyclic loading. At 0.5 Hz, continuous shear softening was observed for all displacement amplitudes. Specifically, the peak shear stresses at amplitudes of 5, 10, and 20 mm decreased from 198.5, 203.6, and 181.6 kPa in the first cycle to 130.7, 130.4, and 128.3 kPa after 60 cycles, respectively (Figure 5a). At higher frequencies (1.0 and 2.0 Hz), the responses at 5 and 10 mm amplitudes generally showed an initial hardening stage followed by progressive softening. For the 5 mm amplitude, the positive-direction maximum shear stress occurred at the third cycle at 1.0 Hz and the fifth cycle at 2.0 Hz. For the 10 mm amplitude, the corresponding maximum occurred at the second and fourth cycles, respectively, followed by progressive softening. In contrast, the 20 mm amplitude exhibited rapid initial shear softening, followed by a gradual recovery in shear resistance toward the end of cyclic loading (Figure 5b,c).

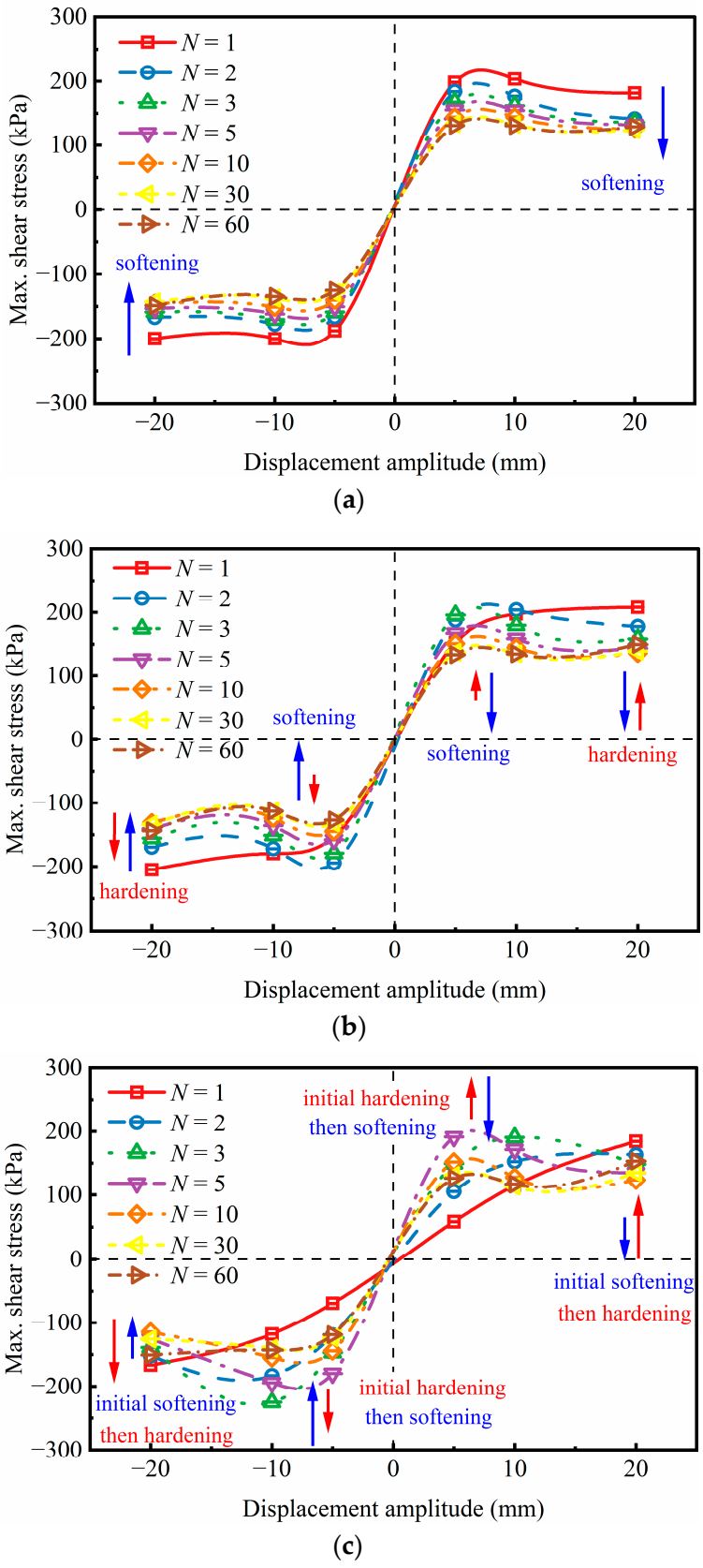

Figure 5. Backbone curves of GMTC–NWGT interface at σ_n = 400 kPa: (**a**) f = 0.5 Hz; (**b**) f = 1.0 Hz; (**c**) f = 2.0 Hz.

3.2. Cyclic Shear Resistance

The peak cyclic shear resistance, τ_p, was defined as the maximum shear stress in the positive loading direction over the 60-cycle sequence, whereas the 60th-cycle cyclic shear resistance, τ_{60}, was defined as the shear stress in the same loading direction during the 60th cycle. The two loading directions were not averaged, and the 60th-cycle strength-retention ratio was calculated as τ_{60}/τ_p. This ratio was used to characterize the relative difference between the maximum measured cyclic shear resistance and the 60th-cycle cyclic shear resistance. Shear resistance for the 27 conditions is presented in Supplementary Table S2.

Figure 6 shows the variation in the 60th-cycle strength-retention ratio with displacement amplitude at a shear frequency of 0.5 Hz, with three curves corresponding to normal stresses of 100, 200 and 400 kPa. The ratio decreased with increasing normal stress, ranging from 0.74–0.84 at 100 kPa, 0.75–0.78 at 200 kPa, and 0.64–0.71 at 400 kPa. The ratio generally decreased as the normal stress increased from 100 kPa to 400 kPa at the same displacement amplitude. The 400 kPa curve remained below the 100 and 200 kPa curves at all displacement amplitudes, indicating a greater reduction in cyclic shear resistance under high normal stress. At 100 kPa, the displacement amplitude had a pronounced effect, and the ratio decreased from 0.84 at 5 mm to 0.74 at 20 mm. This effect weakened at 200 kPa, where the ratio remained nearly stable between 0.75 and 0.78. At 400 kPa, the ratio fluctuated within a narrow range of 0.64–0.71, suggesting that the influence of displacement amplitude became less pronounced under high normal stress.

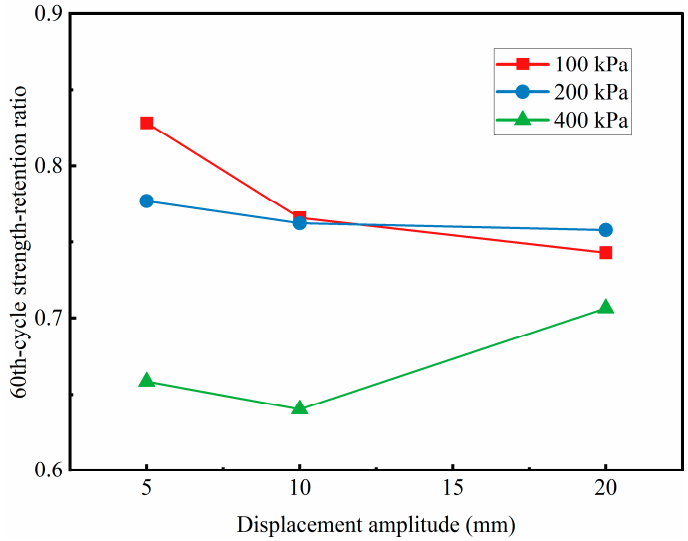

Figure 6. The 60th-cycle strength-retention ratio at different displacement amplitudes and normal stresses.

Figure 7 presents the peak and 60th-cycle cyclic shear resistance envelopes for the GMTC–NWGT interface. The Mohr–Coulomb failure criterion was fitted to the experimental data using linear least-squares regression:

$$\tau_p = c_p + \sigma_n \tan\varphi_p \quad (3)$$

$$\tau_{60} = c_{60} + \sigma_n \tan\varphi_{60} \quad (4)$$

where τ_p and τ_{60} are the peak and 60th-cycle cyclic shear resistances, respectively; c_p and c_{60} are the corresponding apparent cohesions obtained within the tested normal-stress range; and φ_p and φ_{60} are the corresponding fitted friction angles.

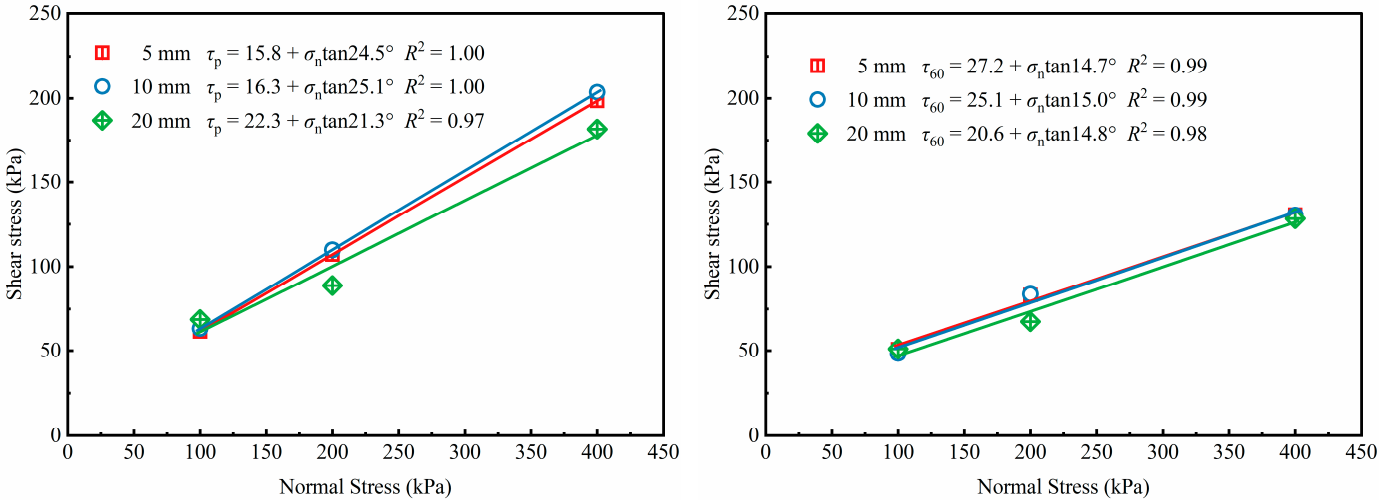

Figure 7. Peak and 60th-cycle cyclic shear resistance envelopes at different displacement amplitudes at f = 0.5 Hz: (**a**) peak cyclic shear resistance; (**b**) 60th-cycle cyclic shear resistance.

The peak and 60th-cycle cyclic shear resistances at f = 0.5 Hz are summarized in Table 3, and the fitted cyclic shear resistance parameters are summarized in Table 4. As shown in Figure 7a, the peak cyclic shear resistance envelopes varied with displacement amplitude. The peak friction angle increased from 24.5° at 5 mm to 25.1° at 10 mm and then decreased to 21.3° at 20 mm. The corresponding apparent cohesion values were 15.8, 16.3, and 22.3 kPa. Figure 7b shows the 60th-cycle cyclic shear resistance envelopes. The 60th-cycle friction angle changed only slightly with displacement amplitude, remaining between 14.7° and 15.0°. The 60th-cycle apparent cohesion decreased from 27.2 kPa at 5 mm to 25.1 kPa at 10 mm and 20.6 kPa at 20 mm.

Table 3. Peak and 60th-cycle cyclic shear resistances at f = 0.5 Hz.

Displacement Amplitude, A (mm)	Normal Stress, σ_n (kPa)	Peak Cyclic Shear Resistance, τ_p (kPa)	60th-Cycle Cyclic Shear Resistance, τ_{60} (kPa)
5	100	61.49	50.92
	200	107.17	83.27
	400	198.48	130.70
10	100	63.19	48.40
	200	109.88	83.77
	400	203.63	130.39
20	100	68.70	51.04
	200	88.89	67.37
	400	181.64	128.30

Table 4. Fitted peak and 60th-cycle cyclic resistance parameters for the tested GMTC–NWGT interface over the normal-stress range of 100–400 kPa at f = 0.5 Hz.

Displacement Amplitude, A (mm)	Peak Friction Angle, φ_p (°)	Peak Apparent Cohesion, c_p (kPa)	Peak Resistance Envelope, R^2 (–)	60th-Cycle Friction Angle, φ_{60} (°)	60th-Cycle Apparent Cohesion, c_{60} (kPa)	60th-Cycle Resistance Envelope, R^2 (–)
5	24.5	15.8	1.00	14.7	27.2	0.99
10	25.1	16.3	1.00	15.0	25.1	0.99
20	21.3	22.3	0.97	14.8	20.6	0.98

3.3. Shear Stiffness and Damping Ratio

Interfacial cyclic secant stiffness and equivalent damping ratio were calculated following the method proposed by Nye and Fox [19].

As illustrated in Figure 8, the secant stiffness was determined separately for the two loading directions to account for possible asymmetry of the hysteresis loop. The directional cyclic secant stiffnesses were defined as:

$$K_1 = \frac{\tau_{m,1}}{A} \tag{5}$$

$$K_2 = \frac{\tau_{m,2}}{A} \tag{6}$$

where K_1 and K_2 are the cyclic secant stiffnesses in the two loading directions; $\tau_{m,1}$ and $\tau_{m,2}$ are the absolute maximum shear stresses in the two loading directions; and A is the prescribed displacement amplitude. The cyclic secant stiffness for the complete cycle was taken as the average of the two directional values:

$$K = \frac{K_1 + K_2}{2} = \frac{\tau_{m,1} + \tau_{m,2}}{2A} \tag{7}$$

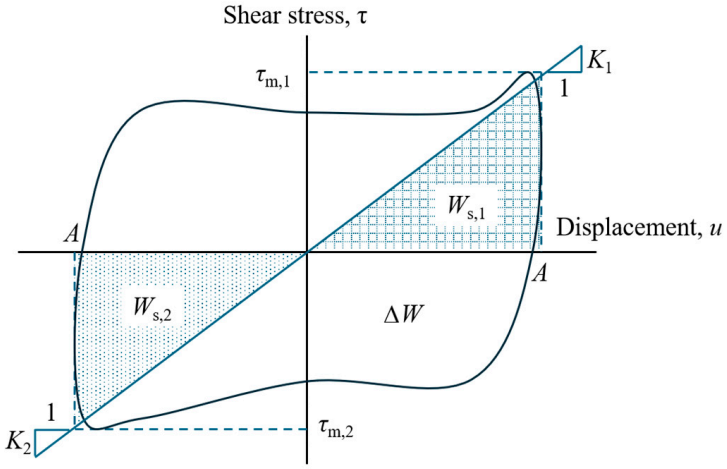

Figure 8. Schematic definition of cyclic secant stiffness and equivalent damping ratio (redrawn and modified from Nye and Fox [19]).

The reference recoverable energies associated with the two loading directions were defined geometrically from the corresponding secant stiffnesses as:

$$W_{s,1} = \frac{1}{2}\tau_{m,1}A \tag{8}$$

$$W_{s,2} = \frac{1}{2}\tau_{m,2}A \tag{9}$$

where $W_{s,1}$ and $W_{s,2}$ are the reference recoverable energies associated with the two loading directions. The damping ratios for the two loading directions were calculated as:

$$\beta_1 = \frac{\Delta W}{4\pi W_{s,1}} \tag{10}$$

$$\beta_2 = \frac{\Delta W}{4\pi W_{s,2}} \tag{11}$$

where β_1 and β_2 are the damping ratios for the two loading directions; ΔW is the energy dissipated during one complete cycle, represented by the area enclosed by the shear stress–

displacement hysteresis loop. The equivalent damping ratio for the complete cycle was taken as the average of the two directional values:

$$\beta = \frac{\beta_1 + \beta_2}{2} = \frac{\Delta W}{4\pi A}\left(\frac{1}{\tau_{m,1}} + \frac{1}{\tau_{m,2}}\right) \quad (12)$$

where β is the equivalent damping ratio for the complete cycle.

For each complete cycle, ΔW was calculated from all shear stress–displacement data points recorded at the 10 ms sampling interval. Positive shear displacement and shear stress were defined in the prescribed positive loading direction. The signed area of the closed hysteresis loop was evaluated numerically from successive sampling points, and the last point of each cycle was connected to the first point to ensure loop closure. The absolute value of the resulting closed-loop integral was taken as the dissipated energy ΔW.

$$\Delta W = \left| \sum_{i=1}^{n-1} \frac{\tau_i + \tau_{i+1}}{2}(u_{i+1} - u_i) + \frac{\tau_n + \tau_1}{2}(u_1 - u_n) \right| \quad (13)$$

where u_i and τ_i are the measured shear displacement and shear stress at the ith sampling point, respectively, and n is the total number of sampling points in one complete cycle. The calculation results of the 27 conditions are presented in Supplementary Tables S3a and S3b.

Figure 9 compares the cyclic secant stiffness at the first and 60th cycles for the tests conducted at f = 0.5 Hz. After 60 cycles, the cyclic secant stiffness decreased by 30–35% across all normal stresses (See the black arrow). Stiffness increased with normal stress and decreased with displacement amplitude. For example, at 400 kPa, initial stiffness dropped from 38.6 kPa·mm^{-1} (5 mm) to 9.5 kPa·mm^{-1} (20 mm), and, after 60 cycles, the corresponding values fell to 26.1 kPa·mm^{-1} and 6.4 kPa·mm^{-1}, respectively. At 100 kPa and the 60th cycle, stiffness decreased by 75% as displacement amplitude increased from 5 mm to 20 mm.

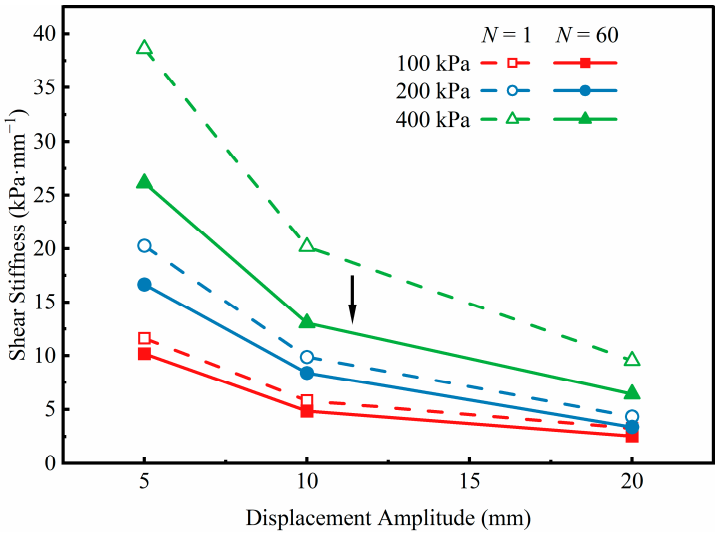

Figure 9. Shear stiffness vs. displacement amplitude of the first and 60th cycles under different normal stresses and displacement amplitudes at f = 0.5 Hz.

Figure 10 shows the variation in damping ratio with test parameters, where Figure 10a represents the damping ratio of the first cycle reaching the preset displacement amplitude, and Figure 10b represents the damping ratio of the 60th (last) cycle. Damping ratio increased monotonically with displacement amplitude under all test conditions, and decreased with increasing shear frequency and rate. At 5 mm amplitude and 100 kPa normal stress, the

initial damping ratio decreased from 0.44 (0.5 Hz) to 0.37 (1.0 Hz) and 0.22 (2.0 Hz), a 50% reduction over the tested frequency range. In addition, the reduction in damping ratio with increasing loading frequency and rate became more pronounced at higher normal stresses. At 2.0 Hz and 20 mm amplitude, the damping ratio increased from 0.34 (100 kPa) to 0.40 (200 kPa) and 0.47 (400 kPa). Comparison of Figure 10a,b shows that the damping ratio of the last cycle was higher than that of the first cycle for most test conditions, although slight decreases were observed under a few conditions. The magnitude of the cycle-dependent change varied with the test conditions rather than showing a consistent dependence on normal stress or shear frequency.

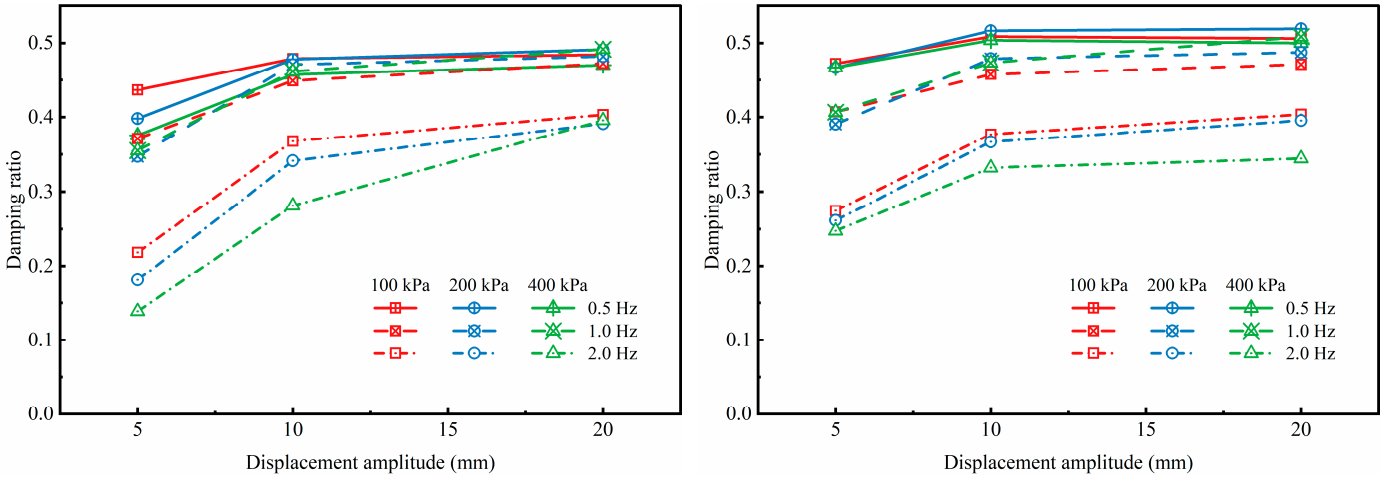

Figure 10. Equivalent damping ratio of the GMTC–NWGT interface: (**a**) damping ratio of the cycle that first reaches the preset displacement amplitude; (**b**) damping ratio of the last cycle.

3.4. Vertical Displacement

Figure 11 shows the vertical displacement–horizontal displacement responses of the GMTC–NWGT interface at σ_n = 400 kPa and A = 20 mm under loading frequencies of 0.5, 1.0, and 2.0 Hz. Positive vertical displacement represents interface compression. At all frequencies, the trajectories gradually shifted toward larger positive vertical displacements with increasing cycles, indicating progressive compressive deformation accumulation. Initial cycles showed limited negative or near-zero displacements, whereas subsequent responses were mainly concentrated between 0.3 and 0.6 mm. Cyclic fluctuations occurred during displacement reversal, with similar overall trends but differences in displacement range and trajectory distribution among the three coupled frequency–velocity conditions.

Figure 12 presents the vertical displacement at the end of each loading cycle. At all frequencies, vertical displacement increased rapidly during the initial ~10 cycles, followed by a slower but continuous accumulation of compressive deformation throughout the remaining cycles. At the 60th cycle, the vertical displacements were approximately 0.48, 0.53, and 0.50 mm for 0.5, 1.0, and 2.0 Hz, respectively. The maximum final displacement occurred at 1.0 Hz, while the values at 0.5 and 2.0 Hz were comparable, indicating a non-monotonic dependence on loading frequency. The continued increase in vertical displacement suggests that the interface had not reached a fully stabilized state by the end of cyclic loading. The vertical displacement measured at the 60th cycle therefore represents the endpoint of the prescribed test rather than a stabilized or residual state.

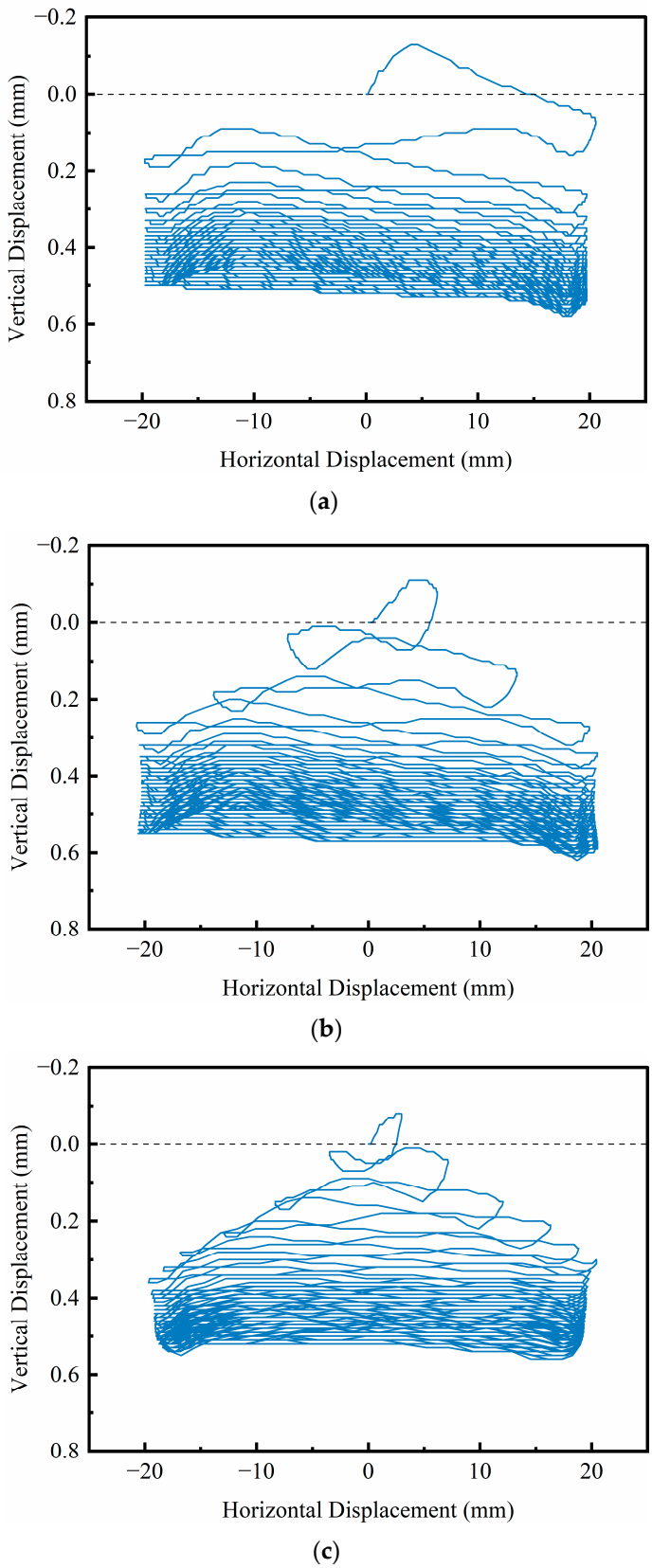

Figure 11. Vertical displacement–horizontal displacement relationships under σ_n = 400 kPa and A = 20 mm: (**a**) 0.5 Hz; (**b**) 1.0 Hz; and (**c**) 2.0 Hz. All 60 complete cycles are shown. Positive vertical displacement denotes compression.

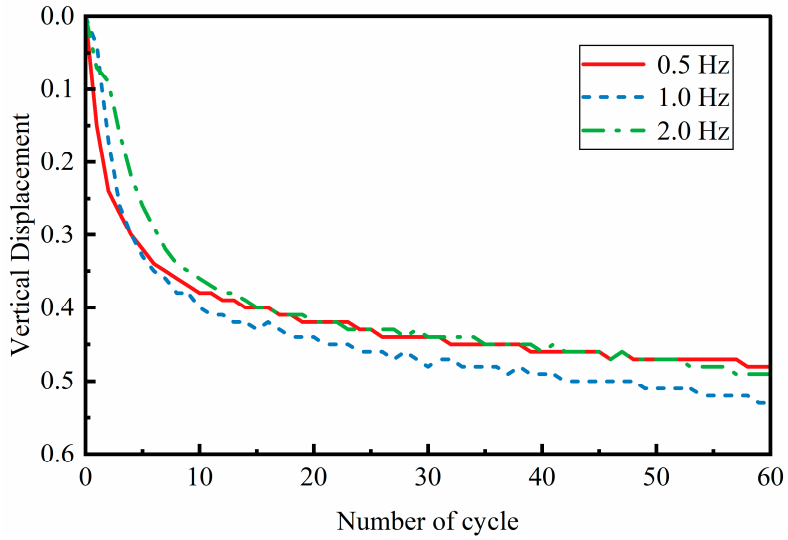

Figure 12. Evolution of cumulative vertical displacement with cycle number under σ_n = 400 kPa and A = 20 mm. Vertical displacement was measured at the completion of each cycle. Positive values denote compression.

4. Discussion of Shear Behavior

Under 400 kPa normal stress and 20 mm displacement amplitude, visible surface changes became more pronounced with shear frequency (GMTC in Figure 13). At 0.5 Hz and 1.0 Hz, detached particles and surface scratching were observed on the GMTC (Figure 13a,b). The extent of visible surface changes increased slightly with frequency, but the overall surface condition remained unchanged. At 2.0 Hz, pronounced fiber attachment was observed between GMTC and NWGT after testing. After specimen separation, a large number of geotextile fibers remained attached to the geomembrane surface (see blue box in Figure 13c). The fiber attachment after testing and late-cycle resistance recovery were observed under the same test condition, but their sequence of occurrence and any causal relationship between them were not established. The mechanical or thermal origin of the observed fiber attachment cannot be determined from the present measurements.

The present study characterizes the cyclic response of the GMTC–NWGT interface as one component of a multilayer liner system. In multilayer configurations, the overall response may be governed by the weakest interface and by interactions among adjacent layers, as reported by Lin et al. [4]. The strength, stiffness, damping, and degradation trends obtained here can therefore provide interface parameters for multilayer stability analyses and help identify the relative contribution of the GMTC–NWGT interface to system performance.

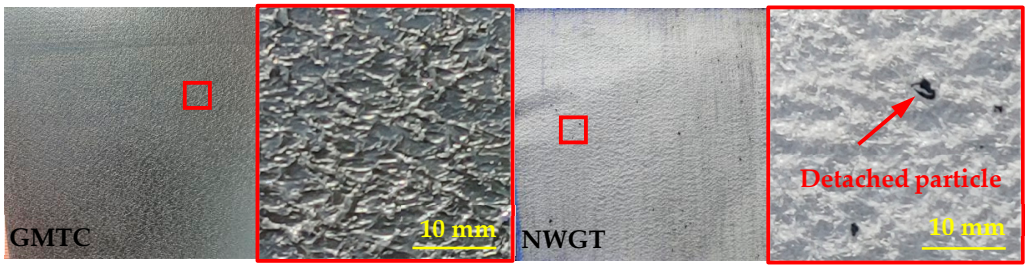

(a)

Figure 13. *Cont.*

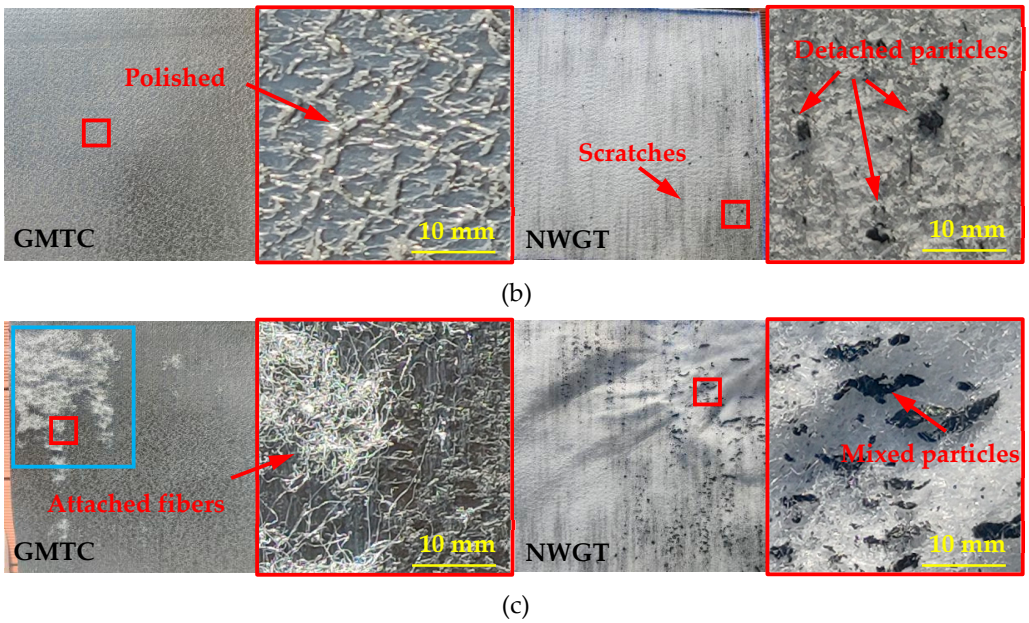

Figure 13. Post-test GMTC and NWGT surfaces after cyclic shearing at σ_n = 400 kPa and A = 20 mm: (**a**) 0.5 Hz; (**b**) 1.0 Hz; and (**c**) 2.0 Hz.

5. Summary and Conclusions

Large-scale horizontal cyclic shear tests were conducted on a GMTC–NWGT interface to investigate the effects of normal stress, displacement amplitude, and shear frequency and corresponding rate across 27 test conditions. The main conclusions are as follows:

(1) The cyclic shear response varied substantially with normal stress. At f = 0.5 Hz, the peak cyclic shear resistance ranged from 61.5–68.7 kPa at a normal stress of 100 kPa and increased to 181.6–203.6 kPa at 400 kPa. The 60th-cycle strength-retention ratio generally decreased with increasing normal stress, indicating a larger relative difference between the maximum measured cyclic shear resistance and the 60th-cycle resistance under higher confinement.

(2) The measured peak cyclic shear resistance varied with displacement amplitude in a normal-stress-dependent manner at f = 0.5 Hz. At 100 kPa, the measured values at 5 and 10 mm were similar, with a higher value at 20 mm. At 200 and 400 kPa, the measured values at 5 and 10 mm were also similar, while lower values were obtained at 20 mm. These trends indicate that normal stress and displacement amplitude should be considered jointly when characterizing the cyclic shear resistance of the interface.

(3) The calculated equivalent damping ratio increased with normal stress and displacement amplitude but decreased with increasing loading frequency and rate, with the frequency- and rate-related reduction becoming more pronounced at higher normal stresses. Accordingly, cyclic secant stiffness and the equivalent damping ratio should be treated as condition-dependent parameters when characterizing the horizontal dynamic shear response of the interface.

(4) Under σ_n = 400 kPa and A = 20 mm, more pronounced post-test fiber attachment and surface changes were observed at 2.0 Hz than at lower frequencies.

Supplementary Materials: The following supporting information can be downloaded at: https://www.mdpi.com/article/10.3390/app16199906/s1, Figure S1: Horizontal displacement-Time history of representative condition(400 kPa, 20mm); Figure S2: Shear force-Time history of representative condition(400 kPa, 20mm); Table S1: Prescribed and measured loading characteristics for all cyclic shear test conditions; Table S2: Positive- and negative-direction cyclic shear resistance and peak-cycle information for all 27 test conditions; Table S3a: Directional secant stiffness, hysteresis-loop area,

reference recoverable energy, and equivalent damping ratio for the first complete cycle after the measured displacement amplitude stabilized at the prescribed value; Table S3b: Directional secant stiffness, hysteresis-loop area, reference recoverable energy, and equivalent damping ratio for the 60th cycle.

Author Contributions: J.H., writing—review and editing, writing—original draft, visualization, validation, supervision, resources, project administration, methodology, investigation, funding acquisition, data curation, and conceptualization. H.F. and Y.M., writing—original draft, visualization, software, investigation, and data curation. All authors have read and agreed to the published version of the manuscript.

Funding: This research was funded by the National Natural Science Foundation of China, grant numbers (52478349, 51978390, 51778353), the Qinghai Provincial Department of Science and Technology International Cooperation Project, grant number (2025-HE-806), the 2023 Basic Research Program of Qinghai Province (2023-ZJ-756), and the China Scholarship Council (CSC 202506890127). The APC was funded by 52478349.

Institutional Review Board Statement: Not applicable.

Informed Consent Statement: Not applicable.

Data Availability Statement: The data presented in this study are available on request from the corresponding author.

Conflicts of Interest: The authors declare no conflicts of interest.

References

1. Feng, S.-J.; Chang, J.-Y.; Shi, H.; Zheng, Q.-T.; Guo, X.-Y.; Zhang, X.-L. Failure of an Unfilled Landfill Cell Due to an Adjacent Steep Slope and a High Groundwater Level: A Case Study. *Eng. Geol.* **2019**, *262*, 105320. [CrossRef]
2. Mitchell, J.K.; Seed, R.B.; Seed, H.B. Kettleman Hills Waste Landfill Slope Failure. I: Liner-System Properties. *J. Geotech. Eng.* **1990**, *116*, 647–668. [CrossRef]
3. Chang, J.-Y.; Feng, S.-J. Dynamic Shear Behaviors of Textured Geomembrane/Nonwoven Geotextile Interface under Cyclic Loading. *Geotext. Geomembr.* **2021**, *49*, 388–398. [CrossRef]
4. Lin, H.; Chen, F.; Liu, Z.; Zheng, W.; Liao, Z.; Shi, J. Experimental Research on Dynamic Shear Characteristics of Multi-layered Geosynthetic Composite Liners. *Chin. J. Geotech. Eng.* **2026**, *48*, 1292–1299. [CrossRef]
5. Tan, Y.; Bradshaw, S.L.; Edil, T.B.; Benson, C.H. Hydraulic Conductivity of Geosynthetic Clay Liners and Compacted Clays to Leachate with PFAS. *J. Geotech. Geoenvironmental Eng.* **2026**, *152*, 04026060. [CrossRef]
6. Pu, G.; Wang, X.; Tian, J.; Shi, L.; Tan, Y.; Chen, L. Geosynthetic Clay Liner for Coal Combustion Product Landfill: An Environmental Impact Assessment. *J. Environ. Manag.* **2025**, *395*, 127886. [CrossRef]
7. Rowe, R.K.; Yu, Y. Magnitude and Significance of Tensile Strains in Geomembrane Landfill Liners. *Geotext. Geomembr.* **2019**, *47*, 439–458. [CrossRef]
8. Brachman, R.W.I.; Sabir, A. Long-Term Assessment of a Layered-Geotextile Protection Layer for Geomembranes. *J. Geotech. Geoenvironmental Eng.* **2013**, *139*, 752–764. [CrossRef]
9. Triplett, E.J.; Fox, P.J. Shear Strength of HDPE Geomembrane/Geosynthetic Clay Liner Interfaces. *J. Geotech. Geoenvironmental Eng.* **2001**, *127*, 543–552. [CrossRef]
10. Jones, D.R.V.; Dixon, N. Shear Strength Properties of Geomembrane/Geotextile Interfaces. *Geotext. Geomembr.* **1998**, *16*, 45–71. [CrossRef]
11. Hou, J.; Xing, X.; Xu, D.; Lu, X. Experimental Study on Dynamic Shear Characteristics of a Geomembrane-Geotextile Interface. *Rock Soil Mech.* **2022**, *43*, 365–376. [CrossRef]
12. Fowmes, G.J.; Dixon, N.; Fu, L.; Zaharescu, C.A. Rapid Prototyping of Geosynthetic Interfaces: Investigation of Peak Strength Using Direct Shear Tests. *Geotext. Geomembr.* **2017**, *45*, 674–687. [CrossRef]
13. Karademir, T.; Frost, J.D. Elevated Temperature Effects on Geotextile–Geomembrane Interface Shear Behavior. *J. Geotech. Geoenvironmental Eng.* **2021**, *147*, 04021148. [CrossRef]
14. Adeleke, D.; Kalumba, D.; Nolutshungu, L.; Oriokot, J.; Martinez, A. The Influence of Asperities and Surface Roughness on Geomembrane/Geotextile Interface Friction Angle. *Int. J. Geosynth. Ground Eng.* **2021**, *7*, 20. [CrossRef]
15. Abdelaal, F.B.; Solanki, R. Effect of Geotextile Ageing and Geomembrane Surface Roughness on the Geomembrane-Geotextile Interfaces for Heap Leaching Applications. *Geotext. Geomembr.* **2022**, *50*, 55–68. [CrossRef]

16. Xu, G.; Shi, J.; Liu, Z.; Zhang, H.; Gu, Y. Angle-Based Residual Strength Estimation of Geotextile/Textured Geomembrane Interface. *Geosynth. Int.* **2025**, *32*, 612–623. [CrossRef]
17. Fowmes, G.J.; Zaharescu, C.A.; Chao, Z.; Mousa, A. Quantification of Shear-Induced Wear Development on Textured Geomembrane-Geotextile Interfaces. *Geotext. Geomembr.* **2026**, *54*, 249–262. [CrossRef]
18. Hou, J.; Xie, X.; Benson, C.H. Effect of Geomembrane Texturing Method on Geomembrane-Dry GCL Interface Shear Behavior. *Geotext. Geomembr.* **2025**, *53*, 1185–1199. [CrossRef]
19. Nye, C.J.; Fox, P.J. Dynamic Shear Behavior of a Needle-Punched Geosynthetic Clay Liner. *J. Geotech. Geoenvironmental Eng.* **2007**, *133*, 973–983. [CrossRef]
20. Cen, W.; Wang, H.; Sun, Y.; Wen, L. Monotonic and Cyclic Shear Behavior of Geomembrane-Sand Interface. *Geosynth. Int.* **2018**, *25*, 369–377. [CrossRef]
21. Chen, A.; Su, C.; Chen, J.; Tang, X.; Yuan, Z. Experimental Study on the Shear Stiffness and Damping Ratio of the Coarse-Grained Soil against Geogrid Interface. *J. Vibroengineering* **2020**, *22*, 1606–1617. [CrossRef]
22. Wang, J.; Shi, J.; Liu, F.; Cai, Y. Effect of Particle Gradation on Static and Dynamic Direct Shear Properties of Geogrid-Sand Interface. *Rock Soil Mech.* **2019**, *40*, 109–117. [CrossRef]
23. Ying, M.; Wang, J.; Liu, F.; Li, J.; Chen, S. Analysis of Cyclic Shear Characteristics of Reinforced Soil Interfaces under Cyclic Loading and Unloading. *Geotext. Geomembr.* **2022**, *50*, 99–115. [CrossRef]
24. Kwak, C.; Park, J.; Jang, D.; Park, I. Dynamic Shear Degradation of Geosynthetic–Soil Interface in Waste Landfill Sites. *Appl. Sci.* **2017**, *7*, 1225. [CrossRef]
25. Wu, J.; Wang, Y.-Q.; Feng, S.-J. Microscale Analysis of Geomembrane–Geotextile Interface Cyclic Shear Behavior Using DEM. *Geotext. Geomembr.* **2025**, *53*, 457–473. [CrossRef]
26. *ASTM D5321/D5321M*; Standard Test Method for Determining the Shear Strength of Soil-Geosynthetic and Geosynthetic-Geosynthetic Interfaces by Direct Shear. ASTM International: West Conshohocken, PA, USA, 2014. [CrossRef]
27. McCartney, J.S.; Zornberg, J.G.; Swan, R.H. Analysis of a Large Database of GCL-Geomembrane Interface Shear Strength Results. *J. Geotech. Geoenvironmental Eng.* **2009**, *135*, 209–223. [CrossRef]
28. Ghazizadeh, S.; Bareither, C.A. Failure Mechanisms of Geosynthetic Clay Liner and Textured Geomembrane Composite Systems. *Geotext. Geomembr.* **2021**, *49*, 789–803. [CrossRef]
29. Athanassopoulos, C.; Fox, P.J.; Ross, J.D. Cyclic Shear Test of a Geosynthetic Clay Liner for a Secondary Containment Application. *Geosynth. Int.* **2010**, *17*, 107–111. [CrossRef]
30. Lo Grasso, S.A.; Massimino, M.R.; Maugeri, M. Dynamic Analysis of Geosynthetic Interfaces by Shaking Table Tests. In *Proceedings of the Geosynthetics—7th ICG*; Swets & Zeitlinger: Lisse, The Netherlands, 2002; Volume 4, pp. 1335–1338.

Disclaimer/Publisher's Note: The statements, opinions and data contained in all publications are solely those of the individual author(s) and contributor(s) and not of MDPI and/or the editor(s). MDPI and/or the editor(s) disclaim responsibility for any injury to people or property resulting from any ideas, methods, instructions or products referred to in the content.